THE JOURNAL OF PHYSICAL CHEMISTRY C
A JOURNAL OF THE AMERICAN CHEMICAL SOCIETY

pubs.acs.org/JPCC
Article

Fluorescence Quenching Driven by PES-Guided Self-Assembly of Ethoxy-Dibenzalacetone and Fullerene-Based Quenchers: A Theoretical and Experimental Study

Vitória M. R. Vasconcelos,* Bruna B. Postacchini, Thiago Cazati, Hélcio S. dos Santos, Andrey Chaves, Valder N. Freire, Cláudia Pessoa, Roner F. da Costa, Igor F. Vasconcelos, and Eveline M. Bezerra

Cite This: J. Phys. Chem. C 2026, 130, 5501−5515

ABSTRACT: Photophysical properties of π-conjugated chromophores are strongly influenced by their molecular environment, which modulates the adiabatic and nonadiabatic energy dissipation. This theoretical and experimental study investigates the chemical reactivity descriptors and potential energy surfaces (PES) underlying the fluorescence quenching of the ethoxy-dibenzalacetone derivative (DBAd) [(1E,4E)-1,5-bis(4-ethoxyphenyl)penta-1,4-dien-3-one] by fullerene-based quenchers (C_{60} and $PC_{61}BM$). Quenching proceeds via the formation of predominantly static and nonfluorescent complexes, supported by linear Stern−Volmer behavior yielding association constants of $(1.83 \pm 0.05) \times 10^4$ and $(2.27 \pm 0.10) \times 10^4$ L·mol^{-1} for C_{60}@DBAd and $PC_{61}BM$@DBAd, respectively, and by an unchanged DBAd excited-state lifetime (~0.20 ns) across quencher concentrations. Förster resonance energy transfer (FRET) contributes more prominently to quenching in $PC_{61}BM$@DBAd, consistent with the larger spectral-overlap integral, whereas photoinduced charge transfer (CT) is comparatively more competitive in C_{60}@DBAd, thermodynamically favored by the HOMO−LUMO alignment at the donor−acceptor interface. PES analyses qualitatively support stable ground-state complexes with stronger short-range stabilization for $PC_{61}BM$@DBAd at intermolecular distances of ~4.9 Å. Overall, DBAd channels excitation to fullerene acceptors through competing nonradiative energy- and charge-transfer pathways, revealing that fluorescence quenching is driven by PES-guided ground-state noncovalent self-assembly and highlighting C_{60}@DBAd and $PC_{61}BM$@DBAd complexes as potentially relevant for organic-fullerene solar cells.

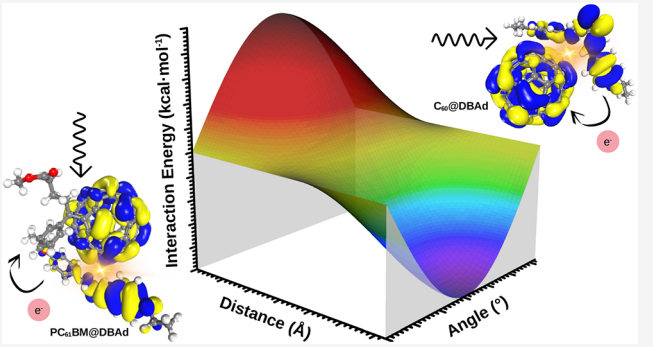

INTRODUCTION

Charge-transfer exciton (CTE) dissociation into free charge carriers at donor−acceptor interfaces is crucial for photocurrent generation in organic-fullerene bulk heterojunction devices.[1] Photoexcited electron−hole pairs exhibit short diffusion lengths and annihilate via photoluminescence emission, thereby limiting photovoltaic efficiency.[2,3] Despite extensive efforts, understanding the mechanisms governing nonradiative CTE dissociation pathways remains a long-standing challenge in organic photovoltaics.[4]

Analogous to Marcus theory, in which electron-transfer efficiency depends on donor−acceptor orbital overlap through short-range exchange interactions that decay exponentially with distance and on the molecular rearrangement energy, CTE dissociation can be described within a similar kinetic framework. In this process, separation requires overcoming the exciton binding energy (E_B) via coupling between donor and acceptor potential energy surfaces (PES).[5,6] Additionally, Förster resonance energy transfer (FRET) allows exciton migration over greater distances (~10−100 Å) through nonradiative dipole−dipole coupling, provided sufficient spectral overlap between donor emission and acceptor absorption.[7,8]

Thermodynamically, the probability of charge separation scales is as follows: $\exp\left(-\frac{E_B}{k_B T}\right)$.[9] Consequently, CTE dissociation is hindered when the electron−hole binding energy (E_B) exceeds the thermal energy ($k_B T$). Enhancing donor−acceptor orbital overlap is therefore crucial for promoting CTE dissociation. In contrast to ionized or hot-carrier states, where excess kinetic energy facilitates charge

Received: November 2, 2025
Revised: February 27, 2026
Accepted: March 2, 2026
Published: March 12, 2026

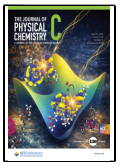

https://doi.org/10.1021/acs.jpcc.5c07504
J. Phys. Chem. C 2026, 130, 5501−5515

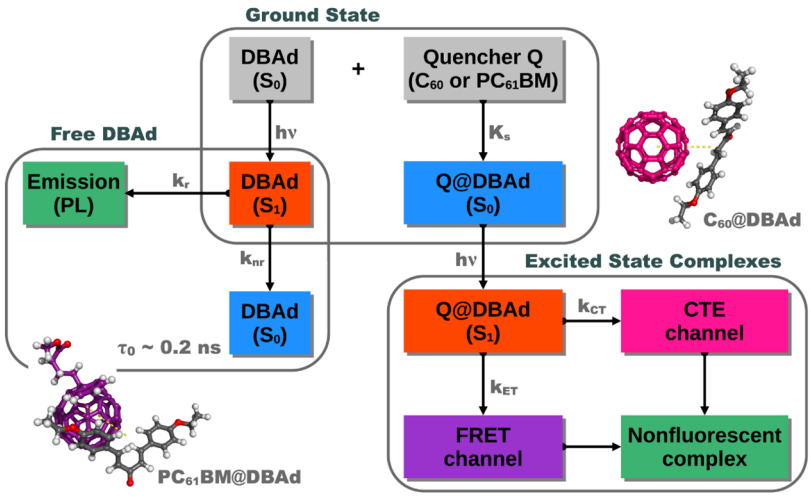

Figure 1. Photophysical and kinetic schemes for fluorescence quenching in DBAd-fullerene donor−acceptor complexes. Free DBAd relaxes from the first electronic state (S_1) via radiative (k_r) and nonradiative (k_{nr}) decay with an excited-state lifetime (τ_0) of approximately 0.2 ± 0.002 ns. Noncovalent ground-state association with the quenchers (C_{60} or $PC_{61}BM$) forms C_{60}@DBAd and $PC_{61}BM$@DBAd complexes characterized by an association constant (K_s). Upon photoexcitation, the preassociated complexes deactivate through charge-transfer exciton (CTE) and Förster resonance energy transfer (FRET) pathways, yielding nonfluorescent states governed by the respective charge and energy transfer rates (k_{CT} and k_{ET}).

separation,[10] the CTE state remains Coulombically bound, with the electron electrostatically confined to the hole.[11]

Fazzi et al.[12] showed that relative molecular orientations critically affect charge-transfer energies, with on-top arrangements enhancing orbital overlap and promoting higher-energy charge transfer, whereas on-edge conformations favor lower-energy transfer. Similarly, Benatto et al.[13] demonstrated that the acceptor position relative to the donor modulates the complex dipole moment and the driving force for electron transfer. These previous studies suggest the central role of the donor−acceptor PES in CTE dissociation and in suppressing exciton recombination losses.[14]

In this work, we combined *ab initio* and molecular mechanics levels of theory to investigate the chemical reactivity descriptors of the ethoxy-dibenzalacetone derivative (DBAd) [(1E,4E)-1,5-bis(4-ethoxyphenyl)penta-1,4-dien-3-one] and fullerene-based acceptors (C_{60} and $PC_{61}BM$), as well as the ground-state classical PES obtained with the universal force field (UFF) for the C_{60}@DBAd and $PC_{61}BM$@DBAd supramolecular complexes, in order to elucidate the fluorescence quenching mechanisms of DBAd. The interaction energies and short-range DBAd-fullerene separations at the ground state qualitatively support the formation of stable donor−acceptor complexes, consistent with the predominantly static quenching scenario revealed by steady-state fluorescence and lifetime analyses.

This theoretical-experimental study has not previously been applied to noncovalently bound DBAd-fullerene complexes. Our analysis shows that, although quantum-chemical reactivity descriptors indicate a more favorable charge-transfer driving force for the C_{60}@DBAd complex, the ground-state PES analysis qualitatively reveals stronger noncovalent interactions and shorter donor−acceptor distances for $PC_{61}BM$@DBAd, consistent with the larger association constant (K_s). Moreover, the PES mapping suggests that the fullerene quencher can already be adjacent to DBAd at the moment of photoexcitation, which is consistent with a predominantly static quenching involving the formation of nonfluorescent complexes, with K_s comparable to those reported for other supramolecular fullerene assemblies.[15,16] Figure 1 summarizes the photophysical and kinetic pathways underlying the fluorescence quenching of DBAd by fullerene acceptors.

COMPUTATIONAL AND EXPERIMENTAL PROCEDURE

Molecular Geometry Optimization

The initial atomic coordinates for the ethoxy-dibenzalacetone derivative (DBAd, [(1E,4E)-1,5-bis(4-ethoxyphenyl)penta-1,4-dien-3-one], PubChem CID 668155[17]) and the fullerene compounds (C_{60} and $PC_{61}BM$) were constructed using ChemCraft[18] and GaussView[19] respectively, as shown in Figure 2. A conformational search was then carried out with the Conformers module of the Biovia Materials Studio[20] software package, using the universal force field (UFF)[21] and a systematic grid scanning method to explore the accessible conformational space of the molecules and identify representative low-energy conformers.

The systematic grid search involved critical torsion angles, with steric filters applied to discard geometries with atomic overlap (or those with severe steric strain) and a smooth cutoff treatment for van der Waals interactions. Low-energy conformers resulting from the search were then subjected to geometric optimization at the molecular mechanics level using the Smart algorithm to minimize within the UFF force field, with convergence criteria reported in Table S1.

Subsequently, density functional theory (DFT) calculations[22,23] were performed on the lowest energy conformer of DBAd, C_{60}, and $PC_{61}BM$ using the DMol^3 module in the Biovia Materials Studio package.[20] These calculations employed the generalized gradient approximation (GGA) with the BLYP exchange-correlation functional[24] complemented by Grimme's dispersion correction (DFT-D)[25] to account for van der Waals interactions. The Kohn−Sham electronic orbitals were expanded using the double numerical plus polarization (DNP+) numerical basis with all-electron calculations (no pseudopotentials). The numerical settings and self-consistent-field (SCF) convergence criteria are summarized in Table S1.

Unconstrained geometry optimizations were performed until the energy- and gradient-based convergence thresholds were satisfied (see Table S1). Harmonic vibrational frequencies of the ground state were calculated using analytical second derivatives within the harmonic approximation in the DMol^3 module of the Biovia Materials Studio[20] software package at the same theoretical level as the DFT geometry optimizations. All optimized structures were confirmed as true

https://doi.org/10.1021/acs.jpcc.5c07504
J. Phys. Chem. C 2026, 130, 5501−5515

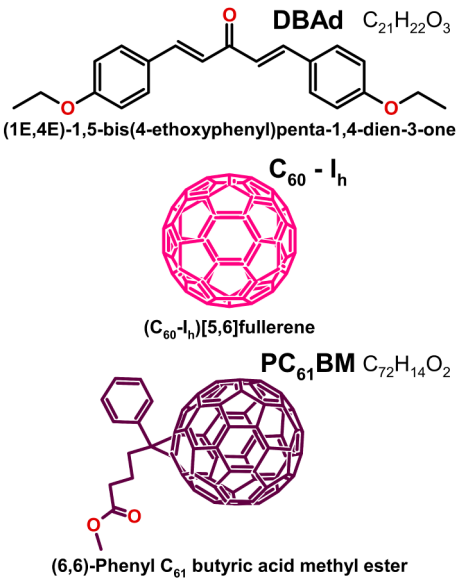

Figure 2. Two-dimensional chemical structure of the ethoxy-dibenzalacetone derivative (DBAd, $C_{21}H_{22}O_3$) and three-dimensional structures of the fullerene compounds (C_{60} and $PC_{61}BM$, $C_{72}H_{14}O_2$) prior to geometry optimization. The carbon atoms of C_{60} and $PC_{61}BM$ are depicted in different colors (C_{60} in pink and $PC_{61}BM$ in purple), whereas hydrogen atoms are not explicitly shown. The structures were created using the ChemCraft program,[18] a graphical tool for visualizing quantum chemistry computations (available at https://www.chemcraftprog.com), and the GaussView program,[19] a graphical interface for Gaussian quantum chemistry computations (available at https://gaussian.com/gaussview6/).

minima on the potential energy surface by the absence of imaginary vibrational modes.

Because pure GGA functionals such as BLYP do not describe long-range dispersion interactions explicitly,[25] an empirical DFT-D correction was included to capture dispersion contributions that are important for π-conjugated and supramolecular complexes.[26] In addition, the DNP+ basis has been reported to provide accuracy comparable to widely used Gaussian double-ζ polarization basis sets for molecular properties at a similar cost.[27] Accordingly, the GGA/BLYP-D2/DNP+ protocol represents a practical compromise between computational cost and accuracy for the ground-state description of DBAd, C_{60}, and $PC_{61}BM$.

Potential Energy Surface (PES) Scanning

The potential energy surface (PES) scanning for the C_{60}@DBAd and $PC_{61}BM$@DBAd supramolecular complexes was carried out using the Forcite module of the Biovia Materials Studio[20] software package. The PES calculations employed the universal force field (UFF)[21] for a qualitative evaluation of the noncovalent interaction energy under nonperiodic conditions, as follows:

$$E^{\text{interaction}}_{(C_{60}@\text{DBAd})} = E_{C_{60}@\text{DBAd}} - (E_{C_{60}} + E_{\text{DBAd}}) \quad (1)$$

and,

$$E^{\text{interaction}}_{(PC_{61}BM@\text{DBAd})} = E_{PC_{61}BM@\text{DBAd}} - (E_{PC_{61}BM} + E_{\text{DBAd}}) \quad (2)$$

where $E^{\text{interaction}}_{(C_{60}@\text{DBAd})}$ and $E^{\text{interaction}}_{(PC_{61}BM@\text{DBAd})}$ are the interaction energies of the complexes C_{60}@DBAd and $PC_{61}BM$@DBAd, respectively, computed from single-point potential energies as the difference between the complex energy and the sum of the isolated-molecule energies; E_{DBAd}, $E_{C_{60}}$, and $E_{PC_{61}BM}$ denote the energies of the isolated DBAd, C_{60}, and $PC_{61}BM$, respectively, evaluated with the same force-field settings as used for the corresponding complex.

Geometric centroids (unweighted averages of the Cartesian coordinates of all atoms, including hydrogens) were first computed for each molecule optimized at the GGA/DFT/BLYP-D2/DNP+ level of theory to define the reference coordinates for the scan. Rigid-body rotations and translations were then systematically explored to map the PES. For the C_{60}@DBAd, due to the topological symmetry of C_{60}, only the DBAd centroid was rotated in 5° increments over 360° and translated up to 30 Å in 0.5 Å steps along each Cartesian axis to achieve a comprehensive spatial sweep.

For the $PC_{61}BM$@DBAd complex, the molecular centroids of DBAd and $PC_{61}BM$ were rotated in 5° and 40° increments over 360°, respectively, while DBAd was translated along each Cartesian axis up to the same cutoff distance of 30 Å in 0.5 Å steps. The Euclidean centroid-to-centroid distance and potential interaction energy between DBAd and the fullerenes were recorded at each rotational-translational step.

Finally, to provide an analytical representation of the interaction potentials obtained from the classical PES scans, the Lennard–Jones (LJ)[28] and Mie[29] functional forms were used to fit $E^{\text{interaction}}_{(C_{60}@\text{DBAd})}$ and $E^{\text{interaction}}_{(PC_{61}BM@\text{DBAd})}$ as a function of the centroid-to-centroid distance. The explicit equations and fitting details are provided in the Tables S2 and S3.

Sample Preparation and Spectroscopic Measurements

The ethoxy-dibenzalacetone derivative (DBAd) [(1E,4E)-1,5-bis(4-ethoxyphenyl)penta-1,4-dien-3-one] was obtained as a powder sample via Claisen–Schmidt condensation. The molecular structure was confirmed by nuclear magnetic resonance (NMR) spectroscopy, with ^{1}H and ^{13}C NMR spectra reported by Oliveira et al.[30] The fullerene compounds (C_{60} and $PC_{61}BM$) were purchased with analytical-grade purity from Merck Sigma-Aldrich.

Initially, stock solutions of C_{60} and $PC_{61}BM$ (7.0×10^{-4} mol·L^{-1}) were prepared in toluene (TOL, $C_6H_5CH_3$), whereas DBAd was prepared in ethanol (EtOH, C_2H_6O) at 1.68×10^{-5} mol·L^{-1}. For each sample, a fixed volume of 2000 μL of the DBAd solution was used. Incremental additions of the C_{60} or $PC_{61}BM$ stock solutions produced quencher concentrations ranging from 1.16×10^{-5} mol·L^{-1} (low concentration, LC) to 10.40×10^{-5} mol·L^{-1} (high concentration, HC); detailed dilutions are provided in Table S6. All solutions were homogenized for 5 min in an ultrasonic bath. The uncertainties of the concentrations were calculated by uncertainty propagation of mass and volume measurements, resulting in the stock solution uncertainty (~5%) being the dominant contribution to the uncertainty of the working solution concentration.

UV–vis absorption spectra over the LC to HC concentration range were recorded using a Shimadzu UV–vis 1900i spectrophotometer at room temperature (25°C) in quartz cuvettes with a 10 mm optical path length, over 280 to 480 nm. Steady-state fluorescence spectra were acquired on a Horiba Fluorolog spectrofluorometer equipped with a xenon lamp, operating in fast acquisition mode with a 0.2 nm sampling interval and 5/5 nm excitation/emission slit widths. DBAd was excited at 365 nm maximum absorption wavelength, and emission spectra were recorded over 300–700 nm.

Time-resolved fluorescence decays were measured by time-correlated single-photon counting (TCSPC) using a FluoTime 200 instrument (PicoQuant). Excitation at 401 nm was provided by a pulsed diode laser operating at a 40 MHz repetition rate. Fluorescence lifetimes were obtained by fitting the decay curves using a sum of exponential functions deconvoluted with the instrument response function (IRF), employing FluoFit software. The quality of the fits was evaluated through analysis of weighted residuals and reduced chi-square (χ^2) values. The detection system consisted of a monochromator coupled to a multichannel plate photomultiplier (Hamamatsu R3809U-50). The excitation pulse width was ~100 ps, resulting in an overall instrumental time resolution of ~64 ps.

Quenching effects were analyzed using the Stern–Volmer[31] relation to distinguish between dynamic (collisional) and static (ground-state complexation) quenching mechanisms[32] as follows:

$$\frac{I_0}{I} = 1 + K[Q] \quad (3)$$

https://doi.org/10.1021/acs.jpcc.5c07504
J. Phys. Chem. C 2026, 130, 5501–5515

where I_0 and I are the steady-state fluorescence intensities of the fluorophore in the absence and presence of the quencher, respectively, [Q] is the quencher concentration, and K is the fluorescence quenching constant.

For collisional quenching, K corresponds to the Stern−Volmer quenching constant (K_{SV}), defined as $K_{SV} = k_q \cdot \tau_0$, where k_q is the bimolecular quenching rate constant and τ_0 is the excited-state lifetime in the absence of a quencher. In this scenario, a decrease in excited-state lifetime is expected, as quenching introduces an additional depopulation pathway for the excited state.[8]

Since purely dynamic (collisional) quenching reduces the steady-state fluorescence intensity and the excited-state lifetime by the same factor, the intensity ratio in (eq 3) can be replaced by the lifetime ratio, τ_0/τ, where τ is the excited-state lifetime in the presence of the quencher. Accordingly,

$$\frac{I_0}{I} = \frac{\tau_0}{\tau} = 1 + k_q\tau_0[Q] \tag{4}$$

In contrast, static quenching arises from the formation of a nonemissive ground-state complex. Under purely static quenching, the lifetime of the uncomplexed (emissive) fluorophore remains unchanged ($\tau = \tau_0$), such that $\tau_0/\tau = 1$, whereas the steady-state intensity decreases with increasing [Q] and the Stern−Volmer constant can be interpreted as an association constant (K_s).[8]

The free energy change for charge transfer (ΔG_{CT}) was estimated using the Rehm−Weller[33] equation, as follows:

$$\Delta G_{CT} = E_{ox} - E_{red} - E_{exc} - \frac{e^2}{4\pi\epsilon_0\epsilon_r r} \tag{5}$$

where E_{ox} is the oxidation potential of the donor (in eV), E_{red} is the reduction potential of the acceptor (in eV), and E_{exc} is the excitation energy of the singlet state of the donor (in eV); e is the elementary charge (1.602×10^{-19} C), ϵ_0 is the vacuum permittivity (8.854×10^{-12} F·m^{-1}), ϵ_r is the relative dielectric constant of the ethanol/toluene (EtOH:TOL) mixture (dimensionless), and r is the average donor−acceptor distance. The dielectric constants of ethanol and toluene under standard conditions were taken from reference,[34] and ϵ_r for the binary mixture was estimated by volumetric averaging using an EtOH:TOL ratio of 2000:400 μL.

The Förster resonance energy transfer (FRET) mechanism was investigated to determine the nonradiative energy transfer rate constants (k_{FRET}) between the donor and acceptor molecules. The k_{FRET} was calculated using the Förster[35] equation:

$$k_{FRET} = \frac{1}{\tau_D}\left(\frac{R_0}{r}\right)^6 \tag{6}$$

where τ_D is the excited-state lifetime of the donor in the absence of the acceptor, R_0 is the Förster radius (the donor−acceptor separation distance at which the transfer efficiency is 50%), and r is the center-to-center distance between the donor and acceptor, calculated here by potential energy surface (PES) scanning.

The Förster radius (R_0, in Å) was determined using the following equation:

$$R_0 = 0.211\left(\frac{\kappa^2\cdot\Phi_D\cdot J(\lambda)}{n^4}\right)^{1/6} \tag{7}$$

where κ^2 is the dipole orientation factor (ranging from 0 to 4, with an isotropic value of 2/3 for freely rotating dipoles[8]), Φ_D is the fluorescence quantum yield of the donor in ethanol in the absence of the acceptor, n is the refractive index for the ethanol-toluene mixture, and $J(\lambda)$ is the spectral overlap integral between the acceptor molar absorptivity coefficient and the area-normalized emission spectrum of the donor, defined as

$$J(\lambda) \equiv \int_0^\infty F_D(\lambda)\varepsilon_A(\lambda)\lambda^4 d\lambda \tag{8}$$

where $F_D(\lambda)$ is the area-normalized fluorescence emission spectrum of the donor, $\varepsilon_A(\lambda)$ is the molar extinction coefficient of the acceptor (in L·mol^{-1}·cm^{-1}), and λ is the wavelength (in nm) corresponding to the spectral overlap region between the donor emission and the acceptor absorption. The refractive index (n) of pure ethanol and toluene under standard conditions was obtained from standard references.[34,36,37] The relative refractive index used in (eq 7) for the binary mixture was calculated as a volumetric average, considering an EtOH:TOL ratio of 2000:400 μL.

The FRET efficiency is quantitatively defined as

$$\eta_{FRET} = \frac{R_0^6}{R_0^6 + r^6} \tag{9}$$

where η_{FRET} represents the fraction of energy transferred from the donor to the acceptor through dipole−dipole interactions.[38] In the present work, r is taken from donor−acceptor conformations inferred from the PES analysis; therefore, η_{FRET} should be interpreted as an upper-bound estimate for the supramolecular complexes rather than as a solvent-averaged efficiency for freely diffusing species in solution. Accordingly, η_{FRET} values indicate that FRET is feasible under compact arrangements but do not imply that FRET is the exclusive or dominant quenching pathway.

RESULTS AND DISCUSSION

Structural and Electronic Properties

Accurate geometric parameters are essential in molecular modeling because they directly influence molecular physicochemical and spectroscopic properties. In this study, the bond lengths and angles of the ethoxy-dibenzalacetone derivative (DBAd) and fullerene compounds (C_{60} and $PC_{61}BM$) were calculated using the GGA-DFT/BLYP/DNP + methodology. The geometric parameters, obtained under nonperiodic boundary conditions, are listed in Table S4 and are organized according to the atomic labeling scheme shown in Figure 3. Geometry optimizations confirmed that all structures correspond to true minima on the potential energy surface, as indicated by the absence of imaginary vibrational frequencies.[39]

Figure S2 and Table S5 show the theoretical Raman activity modes for the optimized structures of DBAd, C_{60}, and $PC_{61}BM$. At the fingerprint region, strong Raman bands at 1571 and 1626 cm^{-1} for DBAd are attributed to the stretching of C═O coupled to C═C stretching modes of the enone fragment.[30] The delocalization induced by π-conjugation results in shifts to lower wavenumbers compared to saturated carbonyls, as also observed by Vasconcelos et al.[41] For fullerenes, DFT/BLYP-D2/DNP+ methodology reproduces high- and low-wavenumber vibrations of the nondegenerate (A_g) and degenerate (H_g) modes and captures C_{60}-cage deformation dynamics.[42] Additionally, the C═O and C═C stretching vibrations at 1720 and 1539 cm^{-1} correspond to the phenyl-butyric acid methyl ester in the $PC_{61}BM$, align with other reports.[43]

After optimizing the geometries of the DBAd, C_{60}, and $PC_{61}BM$, the Kohn−Sham orbitals were expanded to determine the highest occupied molecular orbital (HOMO) and the lowest unoccupied molecular orbital (LUMO) chemical reactivity descriptors.[44] These orbitals play a crucial role in understanding molecular reactivity and charge transfer processes.[23,45] The calculated isosurfaces, shown in Figure 4, represent the spatial distribution of the molecular orbitals. In these isosurfaces, the yellow and blue regions correspond to the positive and negative phases, respectively, indicating the sign of the wave function in different spatial regions.[46]

https://doi.org/10.1021/acs.jpcc.5c07504
J. Phys. Chem. C 2026, 130, 5501−5515

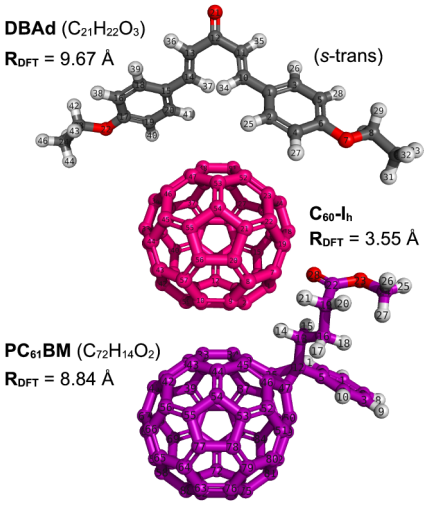

Figure 3. Optimized structures of the ethoxy-dibenzalacetone derivative (DBAd) and fullerene compounds (C_{60} and $PC_{61}BM$) obtained using the GGA/DFT/BLYP-D2/DNP+ level of theory. The structures are represented in ball-and-stick format with atom labels. The carbon atoms of C_{60} and $PC_{61}BM$ are depicted in different colors (C_{60} in pink and $PC_{61}BM$ in purple), while noncarbon atoms are colored according to their atom types (oxygen in red and hydrogen in light gray). The figure was created using PyMOL[40] (PyMOL Molecular Graphics System, available at http://www.pymol.org).

The HOMO/LUMO isosurfaces highlight the electronically dense regions that are most likely to contribute to donor−acceptor electronic coupling through orbital overlap, a crucial process for charge-transfer processes. The isosurfaces also suggest orbital delocalization along the *s-trans* conjugated molecular plane of DBAd and over the icosahedral surface of the fullerene cages (C_{60} and $PC_{61}BM$). Additionally, $PC_{61}BM$ exhibited a slight overlap between the phenyl group and the C_{60} sphere, which was attributed to favorable π-π stacking interactions. These findings align with other studies reported in the literature, such as d'Avino et al.,[47] which states that functionalization in $PC_{61}BM$ induces electronic disorder that affects the distribution of HOMO and LUMO orbitals.

Table 1 shows the values of the HOMO and LUMO energies for DBAd, C_{60}, and $PC_{61}BM$. The HOMO energy values indicate that DBAd predominantly behaves as an electron donor, with a value of −4.95 eV, which is higher than those of C_{60} and $PC_{61}BM$ (−5.46 eV and −5.21 eV, respectively). This difference in HOMO levels suggests that DBAd has a greater propensity to donate electrons compared to the fullerenes.[47,48] Furthermore, the LUMO energy of DBAd (−2.44 eV) is significantly higher than those of C_{60} and $PC_{61}BM$, reflecting a higher energy barrier for electron acceptance.[49] These observations reinforce the role of fullerenes, with their lower LUMO values (−3.79 eV for C_{60} and −3.65 eV for $PC_{61}BM$), as efficient electron acceptors.

Sworakowski[52] experimentally determined the HOMO and LUMO levels of C_{60} at −6.37 eV and −3.99 eV, respectively, based on ultraviolet photoelectron spectroscopy (UPS) and inverse photoelectron spectroscopy (IPES). Shafiq et al.[53] reported that the electronic structure of $PC_{61}BM$ reveals HOMO and LUMO energy levels at −6.10 eV and −3.70 eV, respectively, in good energy-level ordering with GGA/DFT/BLYP-D2/DNP+ level of theory employed herein; see Table 1.

The energy difference between the HOMO level of DBAd and the LUMO level of the fullerenes is 1.16 eV for C_{60} and

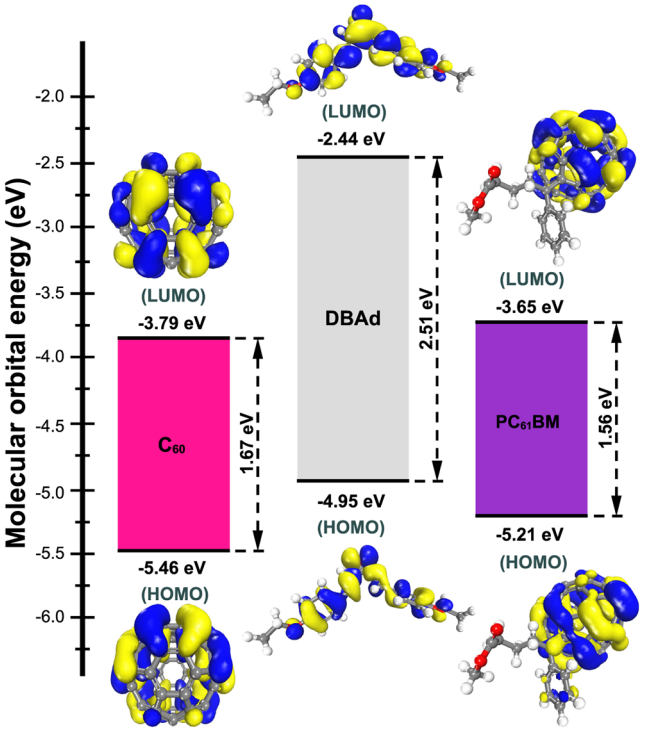

Figure 4. Frontier molecular orbitals energy-level diagram and isosurfaces of the highest occupied molecular orbital (HOMO) and the lowest unoccupied molecular orbital (LUMO) for the ethoxy-dibenzalacetone derivative (DBAd) and fullerene compounds (C_{60} and $PC_{61}BM$) generated with a ± 0.015 isosurface value. The yellow and blue regions represent the positive and negative phases of the molecular orbitals, respectively, indicating the sign of the wave function in different spatial regions. The isosurfaces were generated using Materials Studio[20] (BIOVIA, Dassault Systèmes, available at https://www.3ds.com/products-services/biovia/products/materials-studio/).

Table 1. Highest Occupied Molecular Orbital (HOMO), Lowest Unoccupied Molecular Orbital (LUMO), Ionization Potential (IP), Electron Affinity (EA), Fundamental Energy Gap (E_F), and Experimental Optical Gap (E_{OPT}) Values for the Ethoxy-Dibenzalacetone Derivative (DBAd) and the Fullerene Compounds (C_{60} and $PC_{61}BM$)[a]

	HOMO (eV)	LUMO (eV)	[b]IP (eV)	[c]EA (eV)	[d]E_F (eV)	[e]E_{OPT}^{exp} (eV)
DBAd	−4.95	−2.44	4.95	2.44	2.50	2.9
C_{60}	−5.46	−3.79	5.46	3.79	1.67	3.5
$PC_{61}BM$	−5.21	−3.65	5.21	3.65	1.56	3.4

[a]IP, EA, and E_F descriptors were estimated within Koopman's[50] approximation from the Kohn−Sham frontier orbital energies. [b]Ionization potential (IP = $-E_{HOMO}$) is the energy required to remove an electron from the HOMO. [c]Electron affinity (EA = $-E_{LUMO}$) is the energy released when an electron is added to the LUMO. [d]E_F is the fundamental gap (E_F = IP − EA). [e]Experimental optical gap (E_{OPT}^{exp}) determined using the Tauc plot method,[51] which involves plotting (absorption coefficient vs photon energy)$^{\gamma}$ in (eV·cm^{-1})$^{\gamma}$ against photon energy (in eV) to extrapolate the linear portion to the energy axis. Adopted γ = 2, considering indirect allowed transitions. Data were acquired in a binary ethanol−toluene mixture and expressed with one decimal place due to the resolution of the spectrophotometer.

https://doi.org/10.1021/acs.jpcc.5c07504
J. Phys. Chem. C 2026, 130, 5501−5515

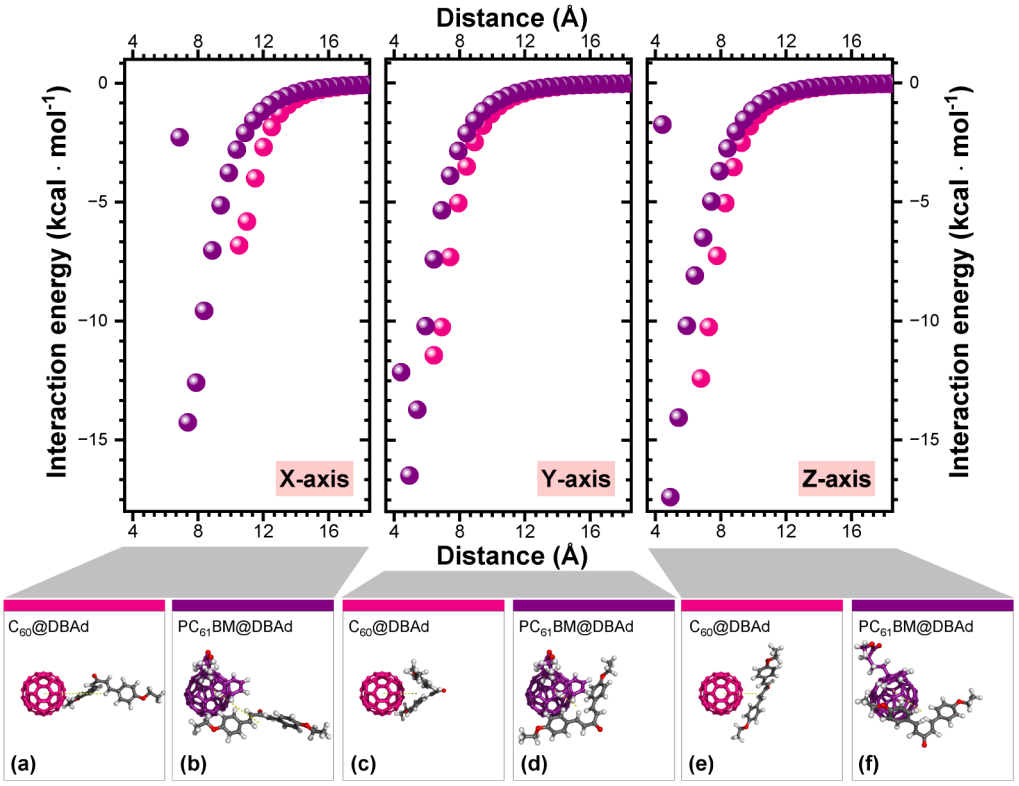

Figure 5. Potential energy surface (PES) mapping of the intermolecular interaction between the ethoxy-dibenzalacetone derivative (DBAd) and fullerene compounds (C_{60} and $PC_{61}BM$) using the Forcite module with the universal force field (UFF).[21] The plots show the interaction energy (kcal·mol^{-1}) as a function of the centroid-to-centroid separation. The minimum-energy conformations identified along each Cartesian axis are also shown, providing insight into the equilibrium configurations and relative stabilization of the DBAd-fullerene complexes.

1.30 eV for $PC_{61}BM$. This larger donor−acceptor offset in the $PC_{61}BM$ complex sets a higher upper bound for the open-circuit voltage (V_{OC}), although the experimentally observed V_{OC} also depends on interfacial energetic losses and nonradiative recombination pathways.[54,55] Therefore, interfacial molecular conformations and donor−acceptor electronic coupling, such as interactions between the icosahedral surface of C_{60} and the π-conjugated molecular plane of DBAd, influence V_{OC} primarily through their impact on nonradiative loss channels.[54−56] Consequently, a larger HOMO−LUMO offset does not necessarily translate into a higher measured V_{OC} if the associated losses are also increased.[54,55]

The frontier orbital energies, as well as the fundamental gap (E_F), are key parameters in understanding the rationalization of charge transfer processes. E_F is defined as the energy difference between the ionization potential (IP) and the electron affinity (EA) and can be approximated by the negative of the HOMO and LUMO energies, respectively, following Koopman's approximation. Another critical parameter is the optical gap (E_{OPT}), which is typically smaller than E_F because E_F describes ionized states, while E_{OPT} is associated with electron−hole bound states, such as excitons.[11,57] These global chemical reactivity descriptors are summarized in Table 1.

Although the E_F of DBAd (2.50 eV) is larger than those of the fullerenes (1.67 eV for C_{60} and 1.56 eV for $PC_{61}BM$), indicating its lower overall reactivity, the ionization potential (IP) of DBAd is lower than that of the fullerenes. This suggests that DBAd requires less energy to lose an electron. Furthermore, the higher EA of the fullerene compounds (3.79 eV for C_{60} and 3.65 eV for $PC_{61}BM$) underscores their strong ability to accept electrons.

Ground-State Noncovalent Interactions

Noncovalent interactions, including dispersion forces (van der Waals and π-π stacking), hydrogen bonding, and dipole−dipole interactions, govern the stability of donor−acceptor assemblies and can influence both ground- and excited-state electronic structure and photophysics.[58] In this study, the intermolecular interactions underlying the potential energy surface (PES) of the ethoxy-dibenzalacetone derivative (DBAd) with the fullerene compounds (C_{60} and $PC_{61}BM$) were qualitatively evaluated at the molecular mechanics level using the universal force field (UFF)[21] parameterized from DFT/BLYP-D2/DNP+ optimized ground-state geometries.

Figure 5 presents the interaction energy profiles (in kcal·mol^{-1}) as a function of the centroid-to-centroid distance (in Å) for the C_{60}@DBAd and $PC_{61}BM$@DBAd complexes, obtained from classical PES scans along the Cartesian axes (x, y, and z). The corresponding minimum-energy conformations identified along each axis are illustrated in subfigures (a)−(f): C_{60}@DBAd for the x, y, and z axis displacements in (a), (c), and (e), respectively, and $PC_{61}BM$@DBAd in (b), (d), and (f). The C_{60}@DBAd and $PC_{61}BM$@DBAd interaction profiles were fitted using Lennard-Jones and Mie potentials to qualitatively capture the balance between attractive and repulsive contributions to the intermolecular potential; see Figure S1 and Tables S2 and S3.

In the C_{60}@DBAd complex, the interaction energy along the x axis is relatively weak, with an estimated value of −6.8 kcal·mol^{-1} at a centroid-to-centroid distance of 10.5 Å. This weaker interaction indicates limited π-π stacking at this separation;[25] see Figure 5 a. The x-axis profile is characterized by longer

https://doi.org/10.1021/acs.jpcc.5c07504
J. Phys. Chem. C 2026, 130, 5501−5515

interaction intervals, highlighting the predominance of weak but long-range attractive forces. Conversely, the $PC_{61}BM$@DBAd complex qualitatively demonstrates a stronger interaction along the x axis, with an interaction energy of −14.3 kcal·mol^{-1} and a reduced centroid-to-centroid distance of 7.4 Å. This enhanced affinity is associated with the butyric acid methyl ester in $PC_{61}BM$, which reduces the icosahedral symmetry of the C_{60}-fullerene cage and introduces local asymmetries in the charge distribution.[47] This functionalization also shifts the center of mass of $PC_{61}BM$ relative to the fullerene cage and enables more anisotropic short-range interactions with the conjugated molecular plane of DBAd.

The intermolecular interactions along the y axis qualitatively show energetically improved conformations. For C_{60}@DBAd, an interaction energy of −11.4 kcal·mol^{-1} is observed at a centroid-to-centroid distance of 6.4 Å. These values indicate favorable molecular docking, where the reduced intermolecular distance enables more effective π-π interactions between the conjugated DBAd and the icosahedral surface of C_{60}. Similarly, the $PC_{61}BM$@DBAd complex suggests an even stronger interaction, with a minimum energy of −16.5 kcal·mol^{-1} at a centroid distance of 5.8 Å. This even shorter centroid distance indicates enhanced van der Waals radius interaction between the DBAd and the functionalized surface of $PC_{61}BM$.[58]

The enhanced short-range interactions along the y axis can suggest increased contributions from dispersive van der Waals forces, which can promote greater delocalization at the DBAd-fullerene donor−acceptor interface. However, despite the reduced distances, the dominant interaction motif is T-shaped rather than purely π-π stacking. This orientation minimizes electrostatic repulsion between the π-systems, favoring energetically more stable interaction geometries.[59] This interaction between topologies is particularly relevant for charge-transfer processes, which facilitate electronic coupling and can promote fast charge separation.[60]

Along the z axis, the C_{60}@DBAd complex exhibits an interaction energy of −12.4 kcal·mol^{-1} at a centroid-to-centroid distance of 6.8 Å. The $PC_{61}BM$@DBAd complex suggests a stronger interaction of −17.4 kcal·mol^{-1} at a slightly reduced centroid-to-centroid distance of 4.9 Å. Although this interaction energy surpasses the values observed along the x and y axes, the relatively larger centroid-to-centroid distance for C_{60}@DBAd along the z axis suggests a dipole−dipole interaction influence with the carbonyl, in addition to the orthogonal (T-shaped) noncovalent.[61] For a detailed comparison, see Figure 5 e and f. The interaction energy and centroid-to-centroid distance corresponding to the lowest-energy conformations along each Cartesian axis are summarized in Table 2.

Although the intermolecular interactions were analyzed exclusively using the universal force field (UFF)[21] π-π stacking is generally recognized as weakened by aromatic inter-ring repulsive forces, especially at short distances.[58,62] Despite this limitation, the quasi-planar conjugated structure of DBAd still permits favorable T-shaped interactions with C_{60}, whereas deeper minima are observed for $PC_{61}BM$@DBAd; see Table 2. Furthermore, while UFF includes Coulomb interactions via assigned partial charges[21] it does not consider polarization or charge redistribution, which limits the description of anisotropic short-range interactions.

In this context, the Lennard-Jones (LJ) and Mie functions were employed as analytical representations of the UFF-derived interaction profiles, enabling an interpretation in terms of the well depth (ϵ), which reflects the relative stabilization at the minimum, and the equilibrium separation (r), which reflects the preferred centroid-to-centroid distance. Such descriptors facilitate comparisons between C_{60}@DBAd and $PC_{61}BM$@DBAd across scan directions, suggesting shorter centroid-to-centroid distances and stronger interaction energies for the $PC_{61}BM$@DBAd complexes. However, LJ showed reduced fitting accuracy, particularly in the repulsive region, whereas Mie provided more consistent correlations for the same profiles; see Tables S2 and S3.

Table 2. Interaction Parameters for the Ethoxy-Dibenzalacetone Derivative (DBAd) with the Fullerene Compounds (C_{60} and $PC_{61}BM$) Obtained from Classical PES Scans Using the Universal Force Field (UFF)[a]

	[b]C_{60}@DBAd			[c]$PC_{61}BM$@DBAd		
Axis[d]	ϵ (kcal·mol^{-1})	r (Å)	E (kcal·mol^{-1})	ϵ (kcal·mol^{-1})	r (Å)	E (kcal·mol^{-1})
X	−6.8	10.5	1144.1	−14.3	7.4	1405.3
Y	−11.4	6.4	1139.5	−16.5	5.8	1403.1
Z	−12.4	6.8	1138.5	−17.4	4.9	1402.2

[a]The table reports the interaction energy (ϵ) in kcal·mol^{-1}, the centroid-to-centroid distance (r) in Å, and the total complex energy (E) in kcal·mol^{-1} for the minimum-energy conformations along the X, Y, and Z displacement directions. [b]Interaction parameters at the minimum-energy points obtained from the Cartesian PES scans for C_{60}@DBAd. [c]Interaction parameters at the minimum-energy points obtained from the Cartesian PES scansfor $PC_{61}BM$@DBAd. [d]X, Y, and Z denote the translation axis used in the PES scan. For each axis, the reported parameters correspond to the most stable configuration (minimum interaction energy) identified over the sampled rigid-body rotations and translations along that axis, and the associated centroid-to-centroid distance. E (kcal·mol^{-1}) denotes the total energy of the complex at the reported minimum.

Additionally, the results provide useful qualitative estimates of the relative conformational stability of the C_{60}@DBAd and $PC_{61}BM$@DBAd complexes, whose methodology aligns with other previous works.[63−65] However, to build on these findings, we recommend further computational studies employing quantum methods. In particular, dispersion-corrected DFT and, where appropriate, optimally tuned range-separated hybrid functionals (OT-RSH) could be used to refine interaction energies and to investigate charge-transfer states in the C_{60}@DBAd and $PC_{61}BM$@DBAd complexes, starting from the equilibrium conformations determined herein.

Fluorescence Quenching and Excited-State Lifetime

Electronic spectra of the ethoxy-dibenzalacetone derivative (DBAd) in the presence of fullerene compounds (C_{60} and $PC_{61}BM$) provide experimental insight into the interaction mechanisms governing these molecular complexes. Figure 6 a and c shows the UV−vis absorption spectra of the C_{60}@DBAd and $PC_{61}BM$@DBAd in ethanol−toluene binary mixtures, respectively. The spectra combine the absorption profile of DBAd (black curve), which exhibits a band centered at 365 nm, with the absorption bands of C_{60} and $PC_{61}BM$ (blue-gray curves) centered around 300 nm. The remaining colored spectra show the evolution of absorbance as a function of increasing concentrations of C_{60} or $PC_{61}BM$, while the DBAd concentration is kept constant at 1.4×10^{-5} mol·L^{-1}. Figure 6 b and d defines the linear working range for C_{60}@DBAd and $PC_{61}BM$@DBAd, considering fullerene concentrations from low (LC) to high (HC) levels.

https://doi.org/10.1021/acs.jpcc.5c07504
J. Phys. Chem. C 2026, 130, 5501−5515

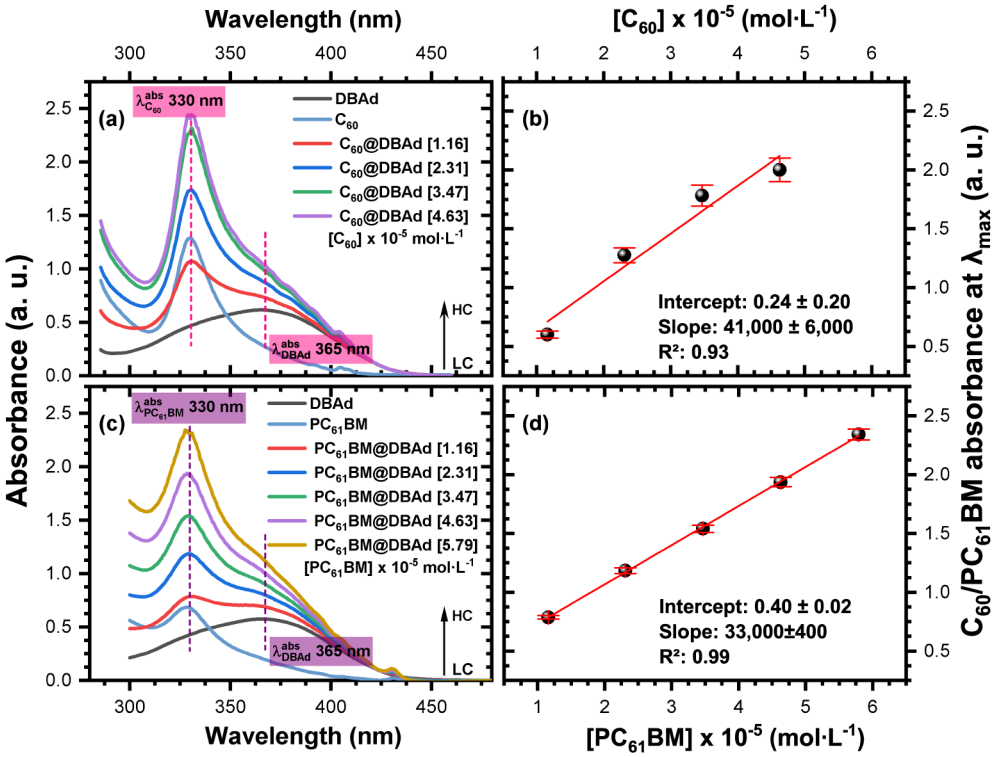

Figure 6. (a) Experimental UV−vis spectra of ethoxy-dibenzalacetone derivative (DBAd), C_{60}, and C_{60}@DBAd at concentrations ranging from low (LC) to high (HC) levels of fullerene. (b) The linear working range for C_{60}@DBAd shows the highest slope (41,000 ± 6,000), indicating rapid saturation of absorbance at concentrations above 4.63×10^{-5} mol·L^{-1}. (c) Experimental UV−vis spectra of DBAd, $PC_{61}BM$, and $PC_{61}BM$@DBAd at varying concentrations from low (LC) to high (HC) levels of functionalized fullerene. (d) The linear working range for $PC_{61}BM$@DBAd exhibits the lowest slope (33,000 ± 400), highlighting the excellent solubility and dispersibility of $PC_{61}BM$@DBAd solutions in the ethanol-toluene mixture.

The subtle shifts in the DBAd maximum absorption wavelength (λ^{abs}_{DBAd}) observed in Figure 6 a and c suggest a perturbation of the DBAd electronic environment upon noncovalent association with C_{60} or $PC_{61}BM$[8,66] consistent with the stronger intermolecular interactions qualitatively predicted by the potential energy surface (PES); see Figure 5 and Table 2. Additionally, no aggregation was observed that could negatively affect the optical absorption of DBAd, except in the case of C_{60}@DBAd at concentrations above 3.47×10^{-5} mol·L^{-1}. At this concentration, the high optical density caused saturation in the absorption spectra, indicating the limited solubility of C_{60} compared to functionalized $PC_{61}BM$; see Figure 6 b and d. This solubility limitation is attributed to the highly hydrophobic surface of C_{60},[67] which impairs effective solvation and interaction with the DBAd chromophore. Furthermore, C_{60} tends to self-associate by noncovalent autoaggregates, hindering its solubility.[68]

Figure 7 a and c shows the steady-state fluorescence spectra of DBAd, excited at 365 nm, in ethanol−toluene binary mixtures containing low (LC) to high (HC) concentrations of the fullerene compounds (C_{60} and $PC_{61}BM$), respectively. The spectra exhibit a linear decrease in DBAd emission as the concentrations of C_{60} and $PC_{61}BM$ progressively increase, indicating a quenching mechanism driven by interactions between DBAd and the fullerene quenchers.[69] However, for C_{60} aliquots exceeding 160 μL (4.63×10^{-5} mol·L^{-1}), the high optical density led to absorbance saturation, compromising the experimental conditions and limiting the linear working range. In contrast, the linearity observed in $PC_{61}BM$@DBAd for all concentration ranges confirms the absence of significant aggregation and highlights the excellent solubility of this functionalized fullerene in the binary solvent mixture. Fluorescence intensity variations at the highest C_{60} and $PC_{61}BM$ concentrations are listed in Figure S3.

DBAd shows measurable photoluminescence in ethanol, whereas no detectable emission is observed in neat toluene under identical instrumental settings. In polar protic media, such as ethanol, solute−solvent interactions (including hydrogen bonding) can restrict conformational freedom and reshape excited-state relaxation channels in α,β-unsaturated carbonyl systems. Moreover, previous solvatochromic analysis of DBAd[41] indicates that a more polar environment stabilizes the dipolar moment of the excited state relative to the ground state, thereby favoring radiative deactivation. Importantly, the ethanol/toluene ratio was kept constant throughout the dilution series (see Table S6); therefore, the observed changes in steady-state fluorescence are attributed to the increasing quencher concentration rather than to variations in solvent composition.

In the binary mixture, DBAd shows an absorption maximum (λ^{abs}_{DBAd}) at 365 nm and an emission maximum (λ^{emi}_{DBAd}) at 485 nm, corresponding to a Stokes shift ($\Delta\tilde{\nu}$) of 6,778 cm^{-1}. The fluorescence quantum yield (Φ_{DBAd}) of DBAd in the same solvent mixture is 0.3%, as determined by a comparative method using Coumarin 6 ($C_{20}H_{18}N_2O_2S$, PubChem CID 100334[70]) in methanol as the reference standard under the same instrumental conditions;[71] the experimental absorption factors and refractive-index correction details are provided in Figure S5.

https://doi.org/10.1021/acs.jpcc.5c07504
J. Phys. Chem. C 2026, 130, 5501−5515

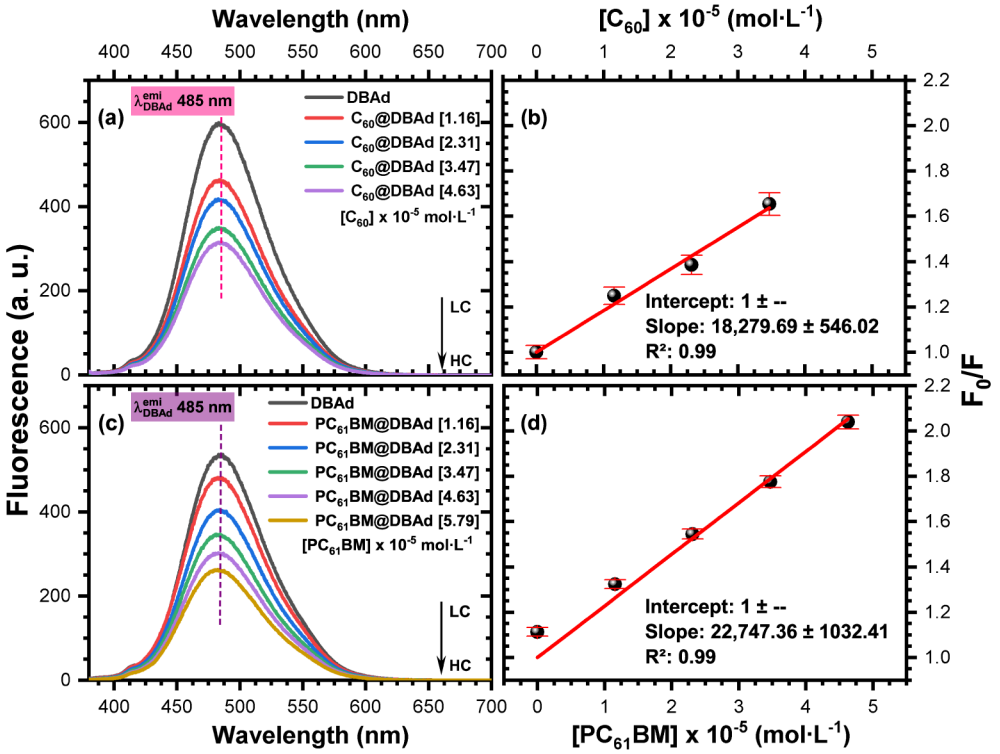

Figure 7. (a) Experimental emission spectra of the ethoxy-dibenzalacetone derivative (DBAd) in the absence and presence of low (LC) to high (HC) concentration aliquots of C_{60}. (b) Stern–Volmer plot for C_{60}@DBAd with an association constant (K_s) of $(1.83 \pm 0.05) \times 10^4$ L·mol^{-1}, where aggregation effects cause minor deviations at higher concentrations. (c) Experimental emission spectra of DBAd in the absence and presence of low (LC) to high (HC) concentration aliquots of $PC_{61}BM$. (d) Stern–Volmer plot for $PC_{61}BM$@DBAd with an association constant (K_s) of $(2.27 \pm 0.10) \times 10^4$ L·mol^{-1}, confirming a linear quenching across the entire concentration range.

Notably, the λ_{DBAd}^{emi} remains unchanged at 485 nm upon increasing the concentration of the C_{60} or $PC_{61}BM$ quenchers (see Figure 7 a and c), indicating that the spectral signature of the emissive DBAd population is preserved within experimental resolution. This detected fluorescence predominantly arises from unassociated DBAd molecules, whereas the quenched fraction is rendered nonemissive through supramolecular association with the fullerene acceptors, followed by efficient nonradiative deactivation. Accordingly, noncovalent interactions govern charge and energy-transfer pathways in these complexes,[8] which exhibit supramolecular short-range stabilization according to the qualitative PES analysis (see Table 2).

Figure 7 b and d shows predominantly linear Stern–Volmer behavior for C_{60}@DBAd and $PC_{61}BM$@DBAd in the ethanol/toluene mixture, with slopes of $(1.83 \pm 0.05) \times 10^4$ and $(2.27 \pm 0.10) \times 10^4$ L·mol^{-1}, respectively. Time-resolved measurements shown in Figure 8 reveal an essentially unchanged DBAd excited-state lifetime (τ) of 0.20 ± 0.002 ns across the quencher concentrations, supporting predominantly static quenching. Accordingly, the Stern–Volmer slopes are interpreted as ground-state association constants (K_s), indicating strong binding and a slightly higher affinity for $PC_{61}BM$ (2.27×10^4 L·mol^{-1}). This trend is consistent with the stronger ground-state noncovalent interactions predicted by the PES analysis (see Table 2). TCSPC decays analyzed by IRF-convoluted exponential fits for all concentration ranges are shown in detail in Figure S4 and summarized in Table S7.

Additionally, the fluorescence decays are well described by a monoexponential fit (short-dashed in Figure 8), indicating that the TCSPC emission can be dominated by a single lifetime

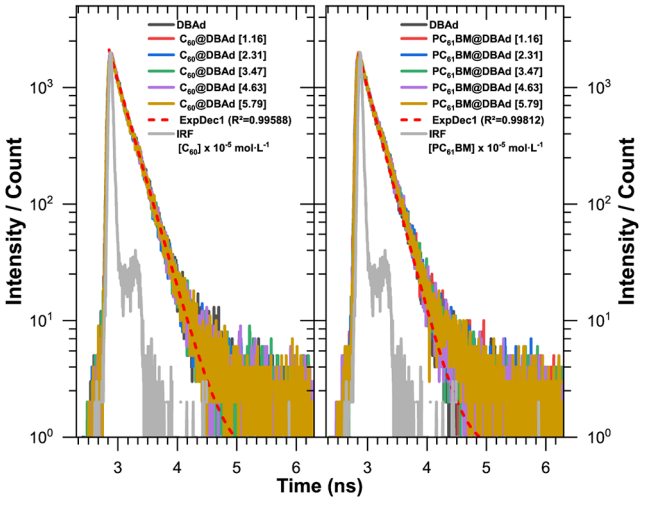

Figure 8. Time-resolved fluorescence decay of DBAd in C_{60}@DBAd (left) and $PC_{61}BM$@DBAd (right) complexes reveals decay lifetimes of approximately 0.20 ns across all quencher concentrations. The absence of systematic variation in the decay lifetimes further supports that the fluorescence quenching mechanism is predominantly static due to ground-state supramolecular complex formation. The short-dashed curves (ExpDec1) represent monoexponential fits to the fluorescence decay profiles, based on the function $I(t) = I_0 \exp\left(-\frac{t}{\tau}\right)$, where $I(t)$ is the fluorescence intensity at time t, I_0 is the initial intensity, and τ is the excited-state lifetime. The good agreement with the monoexponential model indicates the dominance of a single electronic relaxation pathway.

https://doi.org/10.1021/acs.jpcc.5c07504
J. Phys. Chem. C 2026, 130, 5501−5515

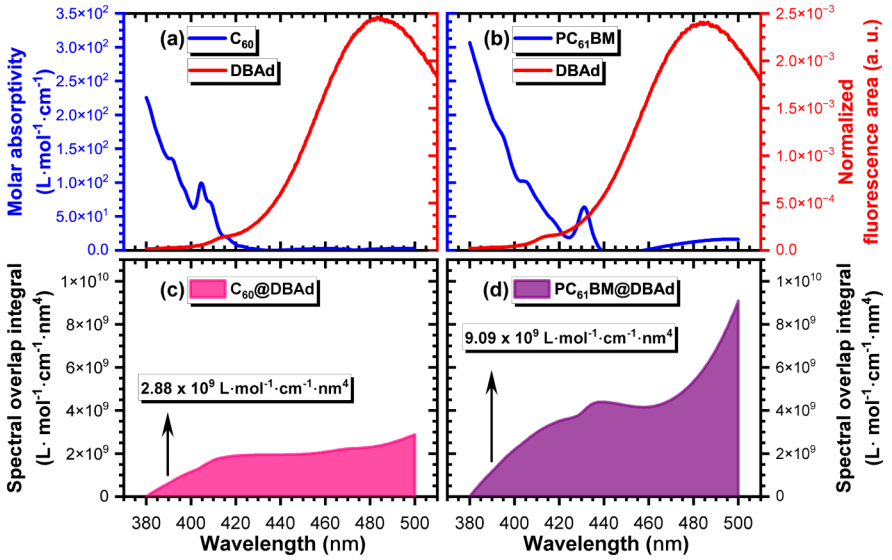

Figure 9. Molar extinction coefficient (ϵ, in L·mol^{-1}·cm^{-1}) of the fullerene acceptors (C_{60} and $PC_{61}BM$), normalized fluorescence emission spectra of DBAd (arbitrary units), and the corresponding spectral overlap integral ($J(\lambda)$ in L·mol^{-1}· cm^{-1}·nm^4) for the C_{60}@DBAd and $PC_{61}BM$@DBAd complexes. (a) C_{60} molar absorptivity and DBAd emission at the same baseline for donor−acceptor overlap. (b) $PC_{61}BM$ molar absorptivity and DBAd emission at the same baseline for donor−acceptor overlap. (c) $J(\lambda)$ for C_{60}@DBAd. (d) $J(\lambda)$ for $PC_{61}BM$@DBAd. Normalization in parts (a) and (b) is applied only for DBAd emission; $J(\lambda)$ was computed using the $\epsilon(\lambda)$ in absolute units and the DBAd emission spectrum normalized to unit area.

under the evaluated experimental conditions. The essentially unchanged lifetime upon increasing quencher concentration is consistent with predominantly static quenching, in agreement with the linear Stern−Volmer behavior (see Figure 7 b and d) and with the favorable ground-state association inferred from PES calculations for C_{60}@DBAd and $PC_{61}BM$@DBAd (see Table 2). This assignment follows the principle that dynamic (collisional) quenching decreases τ, whereas static quenching reduces the steady-state intensity without altering the decay kinetics[8,32] see the details in eqs 3 and 4.

The K_s values found for the DBAd-fullerene complexes are comparable to those reported in previous studies on noncovalently linked assemblies of C_{60}, C_{70}, [6,6]-phenyl-C_{70}-butyric acid methyl-ester, and *tert*-butyl-(1,2-methanofullerene)-61-carboxylate with a designed zinc phthalocyanine (ZnPc) in toluene, which reported K_s values of 6.50×10^3 L·mol^{-1} for C_{60}@ZnPc and 2.22×10^4 L·mol^{-1} for C_{70}@ZnPc.[15] Similar values were also observed for noncovalent donor−acceptor complexes based on (octakis-3,5-di-*tert*-butylphenoxy)phthalocyanine with C_{60} and C_{70}. The bonding constants were 1.2×10^4 L·mol^{-1} for C_{60} and 2.4×10^4 L·mol^{-1} for C_{70}.[16]

Stern−Volmer uncertainties mainly arise from intensity reproducibility and propagate directly to I_0/I and the fitted slope. Still, the regression was restricted to the linear regime used to extract K_s, with fit statistics reported accordingly (see Figure 7); the essentially unchanged DBAd lifetime within experimental uncertainty supports predominantly static quenching, reducing model ambiguity and justifying interpretation of the Stern−Volmer slope as an effective association constant in the accessible concentration range.

Using Φ_{DBAd} and τ_0, the radiative ($k_r = \Phi_{DBAd}/\tau_0$) and nonradiative ($k_{nr} = (1 - \Phi_{DBAd})/\tau_0$) rate constants were estimated as $(1.49 \pm 0.02) \times 10^7$ s^{-1} and $(4.94 \pm 0.07) \times 10^9$ s^{-1}, respectively, indicating that nonradiative deactivation dominates the excited-state decay of DBAd in the ethanol/toluene mixture. Such a large k_{nr} is consistent with efficient internal conversion in flexible π-conjugated chromophores and provides a baseline for interpreting the additional quenching channels introduced upon complexation with C_{60} or $PC_{61}BM$.[72] Corbin et al.[73] reported similar behavior for hydroxylated chalcone derivatives, highlighting that extending conjugation alone is insufficient to suppress nonradiative decay without the presence of conformational rigidity.[72]

Consequently, the predominantly static fluorescence quenching upon increasing fullerene concentrations (see Figure 8) indicates that the dominant deactivation pathways are enabled by preassociated DBAd-fullerene ground-state complexes and are sufficiently efficient to compete within the subnanosecond excited-state lifetime window of DBAd. Because the TCSPC measurements are limited by the instrument response function (IRF) and the short lifetime ($\tau \sim 0.20 \pm 0.002$ ns), processes occurring faster than the instrumental temporal resolution cannot be directly time-resolved here. Nevertheless, the unchanged lifetime across quencher concentrations supports that the quenching contribution is consistent with ground-state complex formation followed by efficient nonradiative deactivation upon excitation.[8,32,74]

The free energy for photoinduced charge transfer (ΔG_{CT}) was estimated using the Rehm−Weller relation (eq 5), combining the oxidation potential of the electron donor DBAd, the reduction potential of the acceptors (C_{60} and $PC_{61}BM$), the relative dielectric constant of the ethanol/toluene binary solvent mixture (ϵ_r = 20.65), and the first singlet−singlet excited-state energy (E_{S1}) of the DBAd fluorophore. The E_{S1} was previously determined by the time-dependent density functional theory (TD-DFT) method within the polarizable continuum model (PCM) solvation.[41]

The E_{S1} is conventionally applied to π-conjugated organic materials to estimate the theoretical optical gap (E_{OPT}^{the}), which approximately corresponds to the vertical excitation from the electronic ground state (S_0) to the first excited state (S_1).[11]

https://doi.org/10.1021/acs.jpcc.5c07504
J. Phys. Chem. C 2026, 130, 5501−5515

Table 3. Förster Resonance Energy Transfer (FRET) Parameters for the Ethoxy-Dibenzalacetone Derivative (DBAd) with Fullerene Compounds (C_{60} and $PC_{61}BM$) at Different Quencher Concentrations[a,b]

	[C_{60}] or [$PC_{61}BM$]	$J(\lambda)$	R_0	k_{FRET}	η_{FRET}
C_{60}@DBAd	1.16	$(6.32 \pm 3.00) \times 10^{11}$	5.37 ± 0.80	$(1.51 \pm 0.72) \times 10^{9}$	0.22 ± 0.09
	2.31	$(3.22 \pm 1.51) \times 10^{11}$	4.80 ± 0.71	$(7.67 \pm 3.61) \times 10^{8}$	0.13 ± 0.06
	3.47	$(2.80 \pm 1.20) \times 10^{11}$	4.72 ± 0.63	$(6.67 \pm 2.88) \times 10^{8}$	0.12 ± 0.05
	4.63	$(3.22 \pm 1.23) \times 10^{11}$	4.86 ± 0.59	$(7.68 \pm 2.94) \times 10^{8}$	0.13 ± 0.05
	5.79	$(3.30 \pm 1.18) \times 10^{11}$	4.89 ± 0.57	$(7.87 \pm 2.81) \times 10^{8}$	0.13 ± 0.04
$PC_{61}BM$@DBAd	1.16	$(7.59 \pm 2.85) \times 10^{11}$	5.59 ± 0.70	$(1.24 \pm 0.47) \times 10^{10}$	0.67 ± 0.16
	2.31	$(3.81 \pm 1.41) \times 10^{11}$	4.99 ± 0.61	$(6.23 \pm 2.31) \times 10^{9}$	0.53 ± 0.15
	3.47	$(2.49 \pm 0.91) \times 10^{11}$	4.65 ± 0.56	$(4.08 \pm 1.48) \times 10^{9}$	0.43 ± 0.13
	4.63	$(1.69 \pm 0.61) \times 10^{11}$	4.36 ± 0.52	$(2.76 \pm 1.00) \times 10^{9}$	0.34 ± 0.11
	5.79	$(1.43 \pm 0.52) \times 10^{11}$	4.24 ± 0.51	$(2.33 \pm 0.85) \times 10^{9}$	0.31 ± 0.10

[a]The parameters include the spectral overlap integral ($J(\lambda)$, in $L \cdot mol^{-1} \cdot cm^{-1} \cdot nm^4$), Förster radius ($R_0$, in Å), Förster transfer rate (k_{FRET}, in s^{-1}), and dimensionless FRET efficiency (η_{FRET}). [b]Values are reported as mean ± standard deviation (SD). The relative standard deviation (RSD) was calculated as RSD(%) = 100 × SD/mean, and the average RSD was obtained by arithmetic averaging over all entries. Across all, $J(\lambda)$ exhibited an average RSD of 39.47%, R_0 showed lower variability with an average RSD of 12.76%, k_{FRET} presented high dispersion with an average RSD of 39.59%, and η_{FRET} displayed substantial relative dispersion with an average RSD of 34.50%. The variability in η_{FRET} is expected because it is a derived quantity and propagates the uncertainties associated with $J(\lambda)$ and R_0 (and the assumed donor−acceptor distance r). Wavelengths (λ) are expressed in nm; consequently, the spectral overlap integral $J(\lambda)$ is reported in $L \cdot mol^{-1} \cdot cm^{-1} \cdot nm^4$. Intermolecular distances, including the donor−acceptor separation r and the Förster radius R_0, are reported in Å (1 nm = 10 Å).

The calculated E_{S1} values reported by Vasconcelos et al.[41] were 3.67 eV in toluene, 3.74 eV in dichloromethane, and 3.76 eV in acetonitrile; therefore, E_{S1} of 3.72 ± 0.05 eV was adopted as a representative excitation energy for the ethanol/toluene mixture. The uncertainty reflects the modest variation of E_{S1} across solvents with distinct dielectric constants within the PCM solvation model.

The ΔG_{CT} values obtained were −2.66 ± 0.05 eV for C_{60}@DBAd and −2.56 ± 0.05 eV for $PC_{61}BM$@DBAd, indicating that photoinduced charge transfer is thermodynamically favorable for both supramolecular complexes, particularly for the C_{60}@DBAd complex due to its lower LUMO energy (−3.79 eV); see Table 1. Comparatively, Curcio et al.[75] reported less negative ΔG_{CT} values of −0.45 eV for C_{60}@DK1 and −0.41 eV for C_{60}@DK2 in C_{60}-difluoroboron β-diketonate assemblies. This difference arises because DBAd exhibits a higher-lying HOMO and a lower HOMO−LUMO gap compared with the DK1 and DK2 derivatives, resulting in a stronger thermodynamic driving force for charge transfer in the DBAd-based complexes.

The Förster resonance energy transfer (FRET) rate constants (k_{FRET}) for the C_{60}@DBAd and $PC_{61}BM$@DBAd were determined using the same method (eq 6). This analysis employed experimentally derived parameters, including the DBAd excited-state lifetime (τ_D) of 0.20 ns and the Förster radius (R_0, in Å) for each complex at the respective fullerene quencher concentrations, calculated (eq 7). The k_{FRET} also considered an isotropic dipole-orientation factor (κ^2) of 2/3, a refractive index (n) of 1.385 for the ethanol/toluene mixture, and the spectral overlap integral ($J(\lambda)$, in $L \cdot mol^{-1} \cdot cm^{-1} \cdot nm^4$) evaluated at each fullerene concentration according to eq 8. The $J(\lambda)$ values were computed from the overlap between the molar extinction coefficient spectra of the fullerene acceptors in absolute units and the DBAd emission spectrum normalized to unit area after the same baseline correction, as shown in Figure 9.

Table 3 summarizes the FRET parameters obtained for DBAd at different fullerene-quencher concentrations. At 1.16 × 10^{-5} mol·L^{-1}, $PC_{61}BM$@DBAd exhibits a higher k_{FRET} (1.24 × 10^{10} s^{-1}) than C_{60}@DBAd (1.51 × 10^{9} s^{-1}), consistent with more efficient dipole−dipole coupling. This trend is supported by the spectral overlap (Figure 9 d) and the shorter donor−acceptor separation inferred from the PES analysis (4.9 Å), both of which increase the FRET probability in the $PC_{61}BM$@DBAd complex. Nascimento et al.[76] determined an R_0 of approximately 33 Å and k_{FRET} of 6.0 × 10^{11} s^{-1} and 3.0 × 10^{12} s^{-1} range, highlighting the fast nature of energy transfer in the coumarin-fullerene donor−acceptor dyads.

Qaiser et al.[77] reported a Förster radius (R_0 of 34 Å for a C_{60}-coumarin C440 donor−acceptor pair and a high transfer efficiency under conditions associated with dimer formation. In the DBAd-fullerene complexes, the calculated FRET parameters are markedly smaller in absolute magnitude: R_0 lies in the 4.24−5.59 Å range (see Table 3), and the corresponding efficiencies (η_{FRET}) are moderate rather than near-unity (∼0.12−0.22 for C_{60}@DBAd and 0.31−0.67 for $PC_{61}BM$@DBAd). Consistently, $PC_{61}BM$@DBAd exhibits larger k_{FRET} values than those of C_{60}@DBAd at all quencher concentrations. The concentration dependence is primarily reflected in the spectral overlap integral, $J(\lambda)$, and hence in R_0: for $PC_{61}BM$@DBAd, both $J(\lambda)$ and R_0 decrease systematically as the quencher concentration increases, whereas for C_{60}@DBAd the values drop at low concentration and then remain approximately constant within uncertainty at higher concentrations. Overall, the results support the idea that Förster-type energy transfer is feasible for both C_{60}@DBAd and $PC_{61}BM$@DBAd; however, they do not establish a FRET-only quenching mechanism. In particular, at subnanometer separations, through-space charge-transfer and exchange-mediated pathways can be competitive with dipole−dipole transfer. A quantitative assessment of such non-FRET contributions would require electronic-structure calculations on the relevant low-energy donor−acceptor configurations.

Finally, both C_{60} and $PC_{61}BM$ exhibit predominantly UV absorption, with intense bands around 330 nm arising from the delocalized π-electrons of the fullerene cage (see Figure 4). This limited spectral coverage restricts direct harvesting of the visible portion of the solar spectrum.[78] Upon supramolecular complexation (C_{60}@DBAd and $PC_{61}BM$@DBAd), DBAd absorbing at 365 nm and transfer the excitation to the fullerene acceptor through competing efficient nonradiative pathways, including Förster energy transfer and photoinduced

https://doi.org/10.1021/acs.jpcc.5c07504
J. Phys. Chem. C 2026, 130, 5501−5515

charge transfer (CT) and/or short-range exchange-Dexter transfer (see Figure 1).

In particular, the larger spectral overlap and higher k_{FRET} values in $PC_{61}BM$@DBAd (see Table 3 and Figure 9) support a Förster contribution in this complex, whereas the thermodynamically favorable driving force for CT and the electronic coupling expected at short donor−acceptor separations indicate that CT/Dexter channels can be comparatively more competitive in C_{60}@DBAd (see Tables 1 and 2). Overall, the coexistence of multiple quenching channels in both assemblies is advantageous for organic solar cells (OSCs), enabling efficient exciton harvesting by the fullerene acceptors and providing additional routes for energy and charge transfer. In this context, such DBAd-fullerene self-assemblies can be combined with broadband UV−visible-absorbing components to extend spectral harvesting and promote charge generation in OSCs.

CONCLUSION

This theoretical and experimental study investigates the ground-state potential energy surface (PES) between the ethoxy-dibenzalacetone derivative (DBAd) and fullerene compounds (C_{60} and $PC_{61}BM$), which form supramolecular complexes not previously investigated and potentially relevant to next-generation organic solar cells. Specifically, the interaction energy (ϵ) and intermolecular distance (r) parameters were analyzed and correlated with the nonradiative pathways of DBAd. Our results demonstrate that fluorescence quenching occurs via a predominantly static mechanism, supported by PES calculations that qualitatively suggest strong noncovalent interactions in the $PC_{61}BM$@DBAd and C_{60}@DBAd complexes. The proximity between donor and acceptor enables efficient excitation energy and photoinduced charge transfer from DBAd to the fullerene acceptors in both assemblies, forming nonfluorescent ground-state complexes, consistent with the unchanged excited-state lifetime of DBAd. $PC_{61}BM$@DBAd exhibits stronger short-range interactions and greater spectral overlap, predominantly enhancing Förster resonance energy transfer (FRET), while C_{60}@DBAd favors charge transfer (CT) due to a more favorable HOMO−LUMO alignment. These findings highlight that combined FRET and CT transfer processes can enhance exciton dissociation and light harvesting in organic-fullerene solar cells. Lastly, this work proposes future studies investigating intermolecular interactions in the excited-state nonequilibrium geometries using advanced quantum molecular dynamics to provide deeper insights into the mechanisms underlying these photophysical processes.

ASSOCIATED CONTENT

Supporting Information

The Supporting Information is available free of charge at https://pubs.acs.org/doi/10.1021/acs.jpcc.5c07504.

Computational parameters (Conformers, DMol^3, Forcite); Lennard−Jones and Mie fitting parameters; optimized geometries; theoretical Raman spectra; concentration profiles; fluorescence decay curves; UV−vis absorption and emission spectra; quantum-yield determination details (PDF)

AUTHOR INFORMATION

Corresponding Author

Vitória M. R. Vasconcelos − *Programa de Pós-Graduação em Engenharia e Ciência de Materiais, Universidade Federal do Ceará (UFC), Fortaleza, Ceará CEP 60440-554, Brasil;* orcid.org/0000-0003-1203-7970; Email: vitoriavasconcelos@alu.ufc.br

Authors

Bruna B. Postacchini − *Departamento de Física, Universidade Federal de Ouro Preto (UFOP), Ouro Preto, Minas Gerais CEP 35400-000, Brasil;* orcid.org/0000-0002-4606-8604

Thiago Cazati − *Departamento de Física, Universidade Federal de Ouro Preto (UFOP), Ouro Preto, Minas Gerais CEP 35400-000, Brasil*

Hélcio S. dos Santos − *Departamento de Química, Universidade Estadual Vale do Acaraú (UVA), Sobral, Ceará CEP 62040-370, Brasil;* orcid.org/0000-0001-5527-164X

Andrey Chaves − *Departamento de Física, Universidade Federal do Ceará (UFC), Fortaleza, Ceará CEP 60440-900, Brasil;* orcid.org/0000-0002-7000-3704

Valder N. Freire − *Departamento de Física, Universidade Federal do Ceará (UFC), Fortaleza, Ceará CEP 60440-900, Brasil*

Cláudia Pessoa − *Programa de Pós-Graduação em Farmacologia, Universidade Federal do Ceará (UFC), Fortaleza, Ceará CEP 60430-275, Brasil*

Roner F. da Costa − *Programa de Pós-Graduação em Ciência e Engenharia de Materiais, Universidade Federal Rural do Semi-árido (UFERSA), Mossoró, Rio Grande do Norte CEP 59625-900, Brasil*

Igor F. Vasconcelos − *Programa de Pós-Graduação em Engenharia e Ciência de Materiais, Universidade Federal do Ceará (UFC), Fortaleza, Ceará CEP 60440-554, Brasil;* orcid.org/0000-0002-6172-805X

Eveline M. Bezerra − *Programa de Pós-Graduação em Ciência e Engenharia de Materiais, Universidade Federal Rural do Semi-árido (UFERSA), Mossoró, Rio Grande do Norte CEP 59625-900, Brasil*

Complete contact information is available at: https://pubs.acs.org/10.1021/acs.jpcc.5c07504

Author Contributions

V.M.R.V., R.F.d.C., I.F.V., and E.M.B. proposed the idea, contributed to the conception and design of the study, planned and carried out the simulations. B.B.P., T.C., V.M.R.V., H.S.d.S., and I.F.V. planned, carried out, and discussed the experimental results, provided critical feedback, cowrote and finalized the manuscript. V.N.F. provided the computer simulation laboratory and software license. B.B.P., T.C., A.C., and C.P. analyzed and discussed the results, provided critical feedback, cowrote and finalized the manuscript. All authors contributed to the manuscript revision and approved the submitted version.

Funding

The Article Processing Charge for the publication of this research was funded by the Coordenacao de Aperfeicoamento de Pessoal de Nivel Superior (CAPES), Brazil (ROR identifier: 00x0ma614).

Notes

The authors declare no competing financial interest.

■ ACKNOWLEDGMENTS

The authors are grateful to the Brazilian research foment agencies: Coordenação de Aperfeiçoamento de Pessoal de Nivel Superior (CAPES), Conselho Nacional de Desenvolvimento Científico e Tecnológico (CNPq), Fundação Cearense de Apoio ao Desenvolvimento Científico e Tecnológico (FUNCAP), Fundação de Amparo à Pesquisa do Estado de Minas Gerais (FAPEMIG), and Instituto Nacional de Ciência e Tecnologia em Eletrônica Orgânica (INCT/INEO) for financial support. R. F. C. acknowledges support from CNPq (Grant No. 102541/2024-8). E. M. B. acknowledges support from FAPERN/CAPES. C. P. acknowledges support from INCT Bio2: Biodescoberta Translacional e Biomodelos (Grant No. 408566/2024-8) and FINEP Mais Inovação Saúde (Contract No. 01.24.0610.00). H. S. S. acknowledges support from CNPq-PQ (Grant No. 306008/2022-0) and FUNCAP-UNIVERSAL (Grant No. UNI-0210-00337.01.00/23). T. C. acknowledges support from CNPq (Grant No. 307341/2021-6). B. B. P. acknowledges institutional support from the Federal University of Ouro Preto (UFOP). I. F. V. acknowledges support from CNPq-PQ (Grant No. 316138/2021-5). A. C. acknowledges support from CNPq-PQ (Grant No. 312705/2022-0). V. M. R. V. acknowledges support from CAPES (Grant No. 88887.501263/2020-00) Financing Code 001, and CNPq-PDJ (Grant No. 112888/2025-9).

■ REFERENCES

(1) Tamai, Y. Charge generation in organic solar cells: Journey toward 20% power conversion efficiency: Special Issue: Emerging Investigators. *Aggregate* **2022**, *3*, No. e280.
(2) Green, M. A. Radiative efficiency of state-of-the-art photovoltaic cells. *Prog. Photovolt: Res. Appl.* **2012**, *20*, 472−476.
(3) Mikhnenko, O. V.; Blom, P. W.; Nguyen, T.-Q. Exciton diffusion in organic semiconductors. *Energy Environ. Sci.* **2015**, *8*, 1867−1888.
(4) Benduhn, J.; Tvingstedt, K.; Piersimoni, F.; Ullbrich, S.; Fan, Y.; Tropiano, M.; McGarry, K. A.; Zeika, O.; Riede, M. K.; Douglas, C. J.; et al. Intrinsic non-radiative voltage losses in fullerene-based organic solar cells. *Nat. Energy* **2017**, *2* (6), 17053.
(5) Knupfer, M. Exciton binding energies in organic semiconductors. *Appl. Phys. A: Mater. Sci. Process* **2003**, *77*, 623−626.
(6) Zhu, L.; Yi, Y.; Wei, Z. Exciton binding energies of nonfullerene small molecule acceptors: Implication for exciton dissociation driving forces in organic solar cells. *J. Phys. Chem. C* **2018**, *122*, 22309−22316.
(7) Medintz, I. L.; Hildebrandt, N. *FRET-Förster resonance energy transfer: From theory to applications*; John Wiley & Sons, 2013.
(8) Lakowicz, J. R. *Principles of Fluorescence Spectroscopy*; 3rd ed.; Springer: New York, NY, USA, 2006.
(9) Zhu, X.-Y.; Yang, Q.; Muntwiler, M. Charge-transfer excitons at organic semiconductor surfaces and interfaces. *Acc. Chem. Res.* **2009**, *42*, 1779−1787.
(10) Cunningham, P. D.; Lane, P. A.; Melinger, J. S.; Esenturk, O.; Heilweil, E. J.; Probing charge transfer and hot carrier dynamics in organic solar cells with terahertz spectroscopy. In *Proceedings of SPIE--the International Society for Optical Engineering*; National Library of Medicine: Bellingham, WA, USA, 2016; Vol.: *9856*, p. 98560Y.
(11) Bredas, J.-L. Mind the gap! *Mater. Horiz.* **2014**, *1*, 17−19.
(12) Fazzi, D.; Barbatti, M.; Thiel, W. Hot and cold charge-transfer mechanisms in organic photovoltaics: Insights into the excited states of donor/acceptor interfaces. *J. Phys. Chem. Lett.* **2017**, *8*, 4727−4734.
(13) Benatto, L.; Sousa, K. R. D. A.; Koehler, M. Driving force for exciton dissociation in organic solar cells: The influence of donor and acceptor relative orientation. *J. Phys. Chem. C* **2020**, *124*, 13580−13591.
(14) Bernardo, B.; Cheyns, D.; Verreet, B.; Schaller, R. D.; Rand, B. P.; Giebink, N. C. Delocalization and dielectric screening of charge transfer states in organic photovoltaic cells. *Nat. Commun.* **2014**, *5* (1), 3245.
(15) Ray, A.; Chattopadhyay, S.; Bhattacharya, S. Photophysical and theoretical insights on non-covalently linked fullerene−zinc phthalocyanine complexes. *Spectrochim. Acta, Part A* **2011**, *79*, 1435−1442.
(16) Ovchenkova, E. N.; Bichan, N. G.; Tsaturyan, A. A.; Lomova, T. N. Non-covalent self-assembly of substituted phthalocyanine with C_{60}, C_{70}, and 9-phenylanthracene: Spectroscopic insights and DFT calculations. *Tetrahedron* **2024**, *162*, 134106.
(17) National Center for Biotechnology Information (NCBI) (1E,4E)-1,5-bis(4-ethoxyphenyl)penta-1,4-dien-3-one; https://pubchem.ncbi.nlm.nih.gov/compound/668155. 2024; Accessed: 15th July 2024.
(18) Chemcraft *Graphical Software for Visualization of Quantum Chemistry Computations*; https://www.chemcraftprog.com. 2018. Accessed: 4th June 2024.
(19) Dennington, R.; Keith, T. A.; Millam, J. M., *GaussView Version 6.0*; https://gaussian.com/gaussview6/. 2019; Accessed: 4th June 2024.
(20) BIOVIA, Dassault Systémes *BIOVIA Discovery Studio Modeling Environment, Version 19.1*; http://www.accelrys.com. 2019; Accessed: 4th June 2024.
(21) RAPPÉ, A. K.; Casewit, C. J.; Colwell, K. S.; Goddard, W. A. I.; Skiff, W. M. UFF, a full periodic table force field for molecular mechanics and molecular dynamics simulations. *J. Am. Chem. Soc.* **1992**, *114*, 10024−10035.
(22) Hohenberg, P.; Kohn, W. Inhomogeneous Electron Gas. *Phys. Rev.* **1964**, *136*, B864−B871.
(23) Kohn, W.; Sham, L. J. Self-Consistent Equations Including Exchange and Correlation Effects. *Phys. Rev.* **1965**, *140*, A1133−A1138.
(24) Becke, A. D. Density-functional exchange-energy approximation with correct asymptotic behavior. *Phys. Rev. A* **1988**, *38*, 3098−3100.
(25) Grimme, S. Semiempirical GGA-type density functional constructed with a long-range dispersion correction. *J. Comput. Chem.* **2006**, *27*, 1787−1799.
(26) Grimme, S. Accurate description of van der Waals complexes by density functional theory including empirical corrections. *J. Comput. Chem.* **2004**, *25*, 1463−1473.
(27) Inada, Y.; Orita, H. Efficiency of numerical basis sets for predicting the binding energies of hydrogen bonded complexes: Evidence of small basis set superposition error compared to Gaussian basis sets. *J. Comput. Chem.* **2008**, *29*, 225−232.
(28) Jones, J. E. On the determination of molecular fields.-II. From the equation of state of a gas. *Proc A* **1924**, *106*, 463−477.
(29) Mie, G. Beiträge zur Optik trüber Medien, speziell kolloidaler Metallösungen. *Annalen der Phys.* **1908**, *330*, 377−445.
(30) de Oliveira, M. M.; Nogueira, C. E. S.; Almeida-Neto, F. W. Q.; Santos, H. S.; Teixeira, A. R.; de Lima-Neto, P.; Marinho, E. S.; de Moraes, M. O.; Pessoa, C.; Barros-Nepomuceno, F. W. A. Full Spectroscopic Characterization and Cytotoxicity Activity of Synthetic Dibenzalacetone Derivatives. *J. Mol. Struct.* **2021**, *1231*, 129670.
(31) Stern, O.; Volmer, M. Über die Abklingungszeit der Fluoreszenz. *Phys. Z.* **1919**, *20*, 183−188.
(32) Valeur, B.; Berberan-Santos, M. N. *Molecular fluorescence: Principles and applications*; John Wiley & Sons: Weinheim, Germany, 2013.
(33) Rehm, D.; Weller, A. Kinetics of fluorescence quenching by electron and H-atom transfer. *Isr. J. Chem.* **1970**, *8*, 259−271.
(34) Wohlfarth, C. *Static Dielectric Constants of Pure Liquids and Binary Liquid Mixtures*; Landolt-Börnstein - Group IV Physical Chemistry, Landolt, M. D. Ed.; Springer: Berlin, Heidelberg, 2017; Vol.: *17B*, pp. 1−945.

https://doi.org/10.1021/acs.jpcc.5c07504
J. Phys. Chem. C 2026, 130, 5501−5515

(35) Förster, T. Zwischenmolekulare energiewanderung und fluoreszenz. *Annalen der Phys.* **1948**, *437*, 55−75.
(36) National Center for Biotechnology Information (NCBI) *Ethanol*; PubChem Compound Summary for CID 702. https://pubchem.ncbi.nlm.nih.gov/compound/Ethanol#section=Odor-Threshold. 2025; Accessed: 12th February 2025.
(37) National Center for Biotechnology Information (NCBI) *Toluene*; PubChem Compound Summary for CID 1140. https://pubchem.ncbi.nlm.nih.gov/compound/Toluene#section=Kovats-Retention-Index. 2025; Accessed: 12th February 2025.
(38) Benatto, L.; Mesquita, O.; Rosa, J. L. B.; Roman, L. S.; Koehler, M.; Capaz, R. B.; Candiotto, G. FRET−Calc: A free software and web server for Förster resonance energy transfer calculation. *Comput. Phys. Commun.* **2023**, *287*, 108715.
(39) Pallikara, I.; Kayastha, P.; Skelton, J. M.; Whalley, L. D. The physical significance of imaginary phonon modes in crystals. *Electron. Struct.* **2022**, *4* (3), 033002.
(40) Schrödinge, LLC *The PyMOL Molecular Graphics System, Version 1.8*; https://pymol.org/. 2015; Accessed: 4th June 2024.
(41) Vasconcelos, V. M. R.; Postacchini, B. B.; dos Santos, H. S.; Cajazeiras, F. F. M.; Freire, V. N.; Junior, C. A.; Pessoa, C.; da Costa, R. F.; Vasconcelos, I. F.; Bezerra, E. M. Red-shifted optical absorption induced by donor−acceptor−donor π-extended dibenzalacetone derivatives. *RSC Adv.* **2025**, *15* (4), 2416−2429.
(42) Schettino, V.; Pagliai, M.; Ciabini, L.; Cardini, G. The vibrational spectrum of fullerene C_{60}. *J. Phys. Chem. A* **2001**, *105*, 11192−11196.
(43) Dresselhaus, M. S.; Dresselhaus, G.; Eklund, P. C. *Science of Fullerenes and Carbon Nanotubes: Their Properties and Applications*; Academic Press: San Diego, CA, 1996; p 965.
(44) Baerends, E.; Gritsenko, O.; Van Meer, R. The Kohn−Sham gap, the fundamental gap and the optical gap: The physical meaning of occupied and virtual Kohn−Sham orbital energies. *Phys. Chem. Chem. Phys.* **2013**, *15*, 16408−16425.
(45) Parr, R. G.; Density-Functional Theory of Atoms and Molecules. In *Horizons of Quantum Chemistry: Proceedings of the Third International Congress of Quantum Chemistry Held at Kyoto, Japan, October 29-November 3, 1979*; Oxford University Press: New York, 1989, pp. 5−15.
(46) Levine, I. N. *Quantum Chemistry*; 6th ed.; Pearson Prentice Hall: Upper Saddle River, NJ, 2009.
(47) d'Avino, G.; Olivier, Y.; Muccioli, L.; Beljonne, D. Do charges delocalize over multiple molecules in fullerene derivatives? *J. Mater. Chem. C* **2016**, *4*, 3747−3756.
(48) Chantrapromma, S.; Ruanwas, P.; Boonnak, N.; Chantrapromma, K.; Fun, H.-K. Synthesis, antityrosinase activity of curcumin analogues, and crystal structure of (1 E, 4E)-1, 5-bis (4-ethoxyphenyl) penta-1, 4-dien-3-one. *Crystallogr. Rep.* **2016**, *61*, 1081−1085.
(49) Brédas, J.-L.; Norton, J. E.; Cornil, J.; Coropceanu, V. Molecular understanding of organic solar cells: The challenges. *Acc. Chem. Res.* **2009**, *42*, 1691−1699.
(50) Koopmans, T. Über die Zuordnung von Wellenfunktionen und Eigenwerten zu den einzelnen Elektronen eines Atoms. *Physica* **1934**, *1*, 104−113.
(51) Tauc, J.; Grigorovici, R.; Vancu, A. Optical properties and electronic structure of amorphous germanium. *Phys. Status Solidi B* **1966**, *15*, 627−637.
(52) Sworakowski, J. How accurate are energies of HOMO and LUMO levels in small-molecule organic semiconductors determined from cyclic voltammetry or optical spectroscopy? *Synth. Met.* **2018**, *235*, 125−130.
(53) Shafiq, A.; Adnan, M.; Hussain, R.; Irshad, Z.; Farooq, U.; Muhammad, S. Molecular engineering of anthracene core-based hole-transporting materials for organic and perovskite photovoltaics. *ACS Omega* **2023**, *8*, 35937−35955.
(54) Gong, X.; Tong, M.; Brunetti, F. G.; Seo, J.; Sun, Y.; Moses, D.; Wudl, F.; Heeger, A. J. Bulk Heterojunction Solar Cells with Large Open-Circuit Voltage: Electron Transfer with Small Donor-Acceptor Energy Offset. *Adv. Mater.* **2011**, *23*, 2272−2277.
(55) Stevens, M. A.; Arango, A. C. Open-circuit voltage exceeding the outermost HOMO−LUMO offset in cascade organic solar cells. *Org. Electron.* **2016**, *37*, 80−84.
(56) Tamura, H.; Tsukada, M. Role of intermolecular charge delocalization on electron transport in fullerene aggregates. *Phys. Rev. B* **2012**, *85* (5), 054301.
(57) Shu, Y.; Truhlar, D. G. Relationships between orbital energies, optical and fundamental gaps, and exciton shifts in approximate density functional theory and quasiparticle theory. *J. Chem. Theory Comput.* **2020**, *16*, 4337−4350.
(58) Grimme, S. Do Special Noncovalent $\pi-\pi$ Stacking Interactions Really Exist? *Angew. Chem. Int. Ed.* **2008**, *47*, 3430−3434.
(59) Hunter, C. A.; Sanders, J. K. The nature of $\pi-\pi$ interactions. *J. Am. Chem. Soc.* **1990**, *112*, 5525−5534.
(60) Scholes, G. D.; Rumbles, G. Excitons in nanoscale systems. *Nat. Mater.* **2006**, *5*, 683−696.
(61) Tsuzuki, S.; Honda, K.; Uchimaru, T.; Mikami, M.; Tanabe, K. Origin of the Attraction and Directionality of the NH/π Interaction: Comparison with OH/π and CH/π Interactions. *J. Am. Chem. Soc.* **2000**, *122*, 11450−11458.
(62) Tsuzuki, S.; Honda, K.; Uchimaru, T.; Mikami, M.; Tanabe, K. Origin of attraction and directionality of the π/π interaction: Model chemistry calculations of benzene dimer interaction. *J. Am. Chem. Soc.* **2002**, *124*, 104−112.
(63) Coelho, M. M.; Bezerra, E. M.; da Costa, R. F.; de Alvarenga, É. C.; Freire, V. N.; Carvalho, C. R.; Pessoa, C.; Albuquerque, E. L.; Costa, R. A. In silico description of the adsorption of cell signaling pathway proteins ovalbumin, glutathione, LC3, TLR4, ASC PYCARD, PI3K and NF-Kβ on 7.0 nm gold nanoparticles: Obtaining their Lennard-Jones-like potentials through docking and molecular mechanics. *RSC Adv.* **2023**, *13*, 35493−35499.
(64) Frazao, N. F.; Albuquerque, E. L.; Fulco, U. L.; Azevedo, D. L.; Mendonça, G. L.; Lima-Neto, P.; Caetano, E. W.; Santana, J. V.; Freire, V. N. Four-level levodopa adsorption on C_{60} fullerene for transdermal and oral administration: A computational study. *RSC Adv.* **2012**, *2*, 8306−8322.
(65) Hadad, A.; Azevedo, D. L.; Caetano, E. W.; Freire, V. N.; Mendonca, G. L.; Neto, P. L.; Albuquerque, E. L.; Margis, R.; Gottfried, C. Two-level adsorption of ibuprofen on C_{60} fullerene for transdermal delivery: Classical molecular dynamics and density functional theory compu tations. *J. Phys. Chem. C* **2011**, *115*, 24501−24511.
(66) Tomin, V. I.Physical principles behind spectroscopic response of organic fluorophores to intermolecular interactions*Advanced Fluorescence Reporters In Chemistry And Biology I: Fundamentals And Molecular Design*Demchenko, A.SpringerBerlin, Heidelberg20108189−223
(67) Li, J.; Chen, M.; Zhou, S.; Li, H.; Hao, J. Self-assembly of fullerene C_{60}-based amphiphiles in solutions. *Chem. Soc. Rev.* **2022**, *51*, 3226−3242.
(68) Sabirov, D. S.; Ori, O.; Tukhbatullina, A. A.; Shepelevich, I. S. Covalently bonded fullerene nano-aggregates $(C_{60})_n$: Digitalizing their energy−topology−symmetry. *Symmetry* **2021**, *13* (10), 1899.
(69) Elistratova, M. A.; Koroleva, M. O.; Zakharova, I. B.Fluorescence Quenching of Tetraphenylporphyrin-Fullerene Molecular Complexes*International Youth Conference on Electronics, Telecommunications And Information Technologies*-Springer2021255247−253
(70) National Center for Biotechnology Information (NCBI) *Coumarin 6*; PubChem Compound Summary for CID 5315457, https://pubchem.ncbi.nlm.nih.gov/compound/Coumarin-6. 2024; Accessed: 10 June 2025.
(71) Brouwer, A. M. Standards for photoluminescence quantum yield measurements in solution. *Pure Appl. Chem.* **2011**, *83*, 2213−2228.
(72) Nelson, T. R.; White, A. J.; Bjorgaard, J. A.; Sifain, A. E.; Zhang, Y.; Nebgen, B.; Fernandez-Alberti, S.; Mozyrsky, D.; Roitberg, A. E.;

https://doi.org/10.1021/acs.jpcc.5c07504
J. Phys. Chem. C 2026, 130, 5501−5515

Tretiak, S. Non-adiabatic excited-state molecular dynamics: Theory and applications for modeling photophysics in extended molecular materials. *Chem. Rev.* **2020**, *120*, 2215−2287.
(73) Corbin, B.; Houglan, P.; Pang, Y. Fluorescence of 2-Hydroxy Chalcone Analogs with Extended Conjugation: ESIPT vs. ICT Pathways. *Molecules* **2024**, *29*, 5972.
(74) Kimber, P.; Plasser, F. Energy component analysis for electronically excited states of molecules: Why the lowest excited state is not always the HOMO/LUMO transition. *J. Chem. Theory Comput.* **2023**, *19*, 2340−2352.
(75) Curcio, S. F.; Carvalho, G. L.; Paez, E. B. A.; Neme, N. P.; Valaski, R.; Matos, M. J. S.; Taylor, J. G.; Cazati, T. Exploring photophysical behavior and fullerene-induced quenching in Difluoroboron Flavanone β-Diketonates for application in organic electronic devices: Experimental and Theoretical Analysis. *Mater. Today Commun.* **2024**, *41*, 110878.
(76) Nascimento, S.; Fedorov, A.; Brites, M. J.; Berberan-Santos, M. N. New coumarin-[60] fullerene dyads connected by an alkynyl linkage: Synthesis and fluorescence studies. Evidence for efficient singlet−singlet energy transfer. *Dyes Pigm.* **2015**, *114*, 158−165.
(77) Qaiser, D.; Khan, M. S.; Singh, R.; Khan, Z. H.; Chawla, S. Förster's resonance energy transfer between Fullerene C_{60} and Coumarin C440. *Spectrochim. Acta, Part A* **2010**, *77*, 1065−1068.
(78) Ganesamoorthy, R.; Sathiyan, G.; Sakthivel, P. Fullerene based acceptors for efficient bulk heterojunction organic solar cell applications. *Sol. Energy Mater. Sol. Cells* **2017**, *161*, 102−148.

https://doi.org/10.1021/acs.jpcc.5c07504
J. Phys. Chem. C 2026, 130, 5501−5515